Development of real-time plasma analysis and control algorithms for the TCV tokamak using SIMULINK

F. Felici [a,b,*], H.B. Le [a], J.I. Paley [a], B.P. Duval [a], S. Coda [a], J.-M. Moret [a], A. Bortolon [a], L. Federspiel [a], T.P. Goodman [a], G. Hommen [e,b], A. Karpushov [a], F. Piras [a], A. Pitzschke [a], J. Romero [c], G. Sevillano [d], O. Sauter [a], W. Vijvers [a], the TCV Team

[a] École Polytechnique Fédérale de Lausanne (EPFL), Centre de Recherches en Physique des Plasmas, Association EURATOM-Suisse, 1015 Lausanne, Switzerland
[b] Eindhoven University of Technology, Department of Mechanical Engineering, Control Systems Technology Group, P.O. Box 513, 5600MB Eindhoven, The Netherlands
[c] National Laboratory of Fusion, EURATOM-CIEMAT, Madrid, Spain
[d] Department of Automatic Control and Systems Engineering, Bilbao University of the Basque Country, Bilbao, Spain
[e] FOM-Institute DIFFER, Association EURATOM-FOM, Nieuwegein, The Netherlands

HIGHLIGHTS

- A new digital control system for the TCV tokamak has been commissioned.
- The system is entirely programmable by SIMULINK, allowing rapid algorithm development.
- Different control system nodes can run different algorithms at varying sampling times.
- The previous control system functions have been emulated and improved.
- New capabilities include MHD control, profile control, equilibrium reconstruction.

ARTICLE INFO

ABSTRACT

One of the key features of the new digital plasma control system installed on the TCV tokamak is the possibility to rapidly design, test and deploy real-time algorithms. With this flexibility the new control system has been used for a large number of new experiments which exploit TCV's powerful actuators consisting of 16 individually controllable poloidal field coils and 7 real-time steerable electron cyclotron (EC) launchers. The system has been used for various applications, ranging from event-based real-time MHD control to real-time current diffusion simulations. These advances have propelled real-time control to one of the cornerstones of the TCV experimental program. Use of the SIMULINK graphical programming language to directly program the control system has greatly facilitated algorithm development and allowed a multitude of different algorithms to be deployed in a short time. This paper will give an overview of the developed algorithms and their application in physics experiments.

© 2013 Elsevier B.V. All rights reserved.

1. Introduction

With the continuing increase of computing power and reduction of costs of digital control hardware, most fusion devices have migrated to fully digital technologies for their plasma control systems. This has greatly resulted in increased capabilities and flexibility of such systems and hence the possible applications. Plasma control is now at the forefront of many tokamaks' research priorities in view of ITER, which will heavily rely on advanced control for safe operation. In 2008, it was decided to develop a new digital control system in the TCV tokamak [1] (major and minor radii 0.88 m and 0.25 m, plasma current up to 1 MA, toroidal magnetic field up to 1.5 T, up to 4.5 MW auxiliary heating and current drive from second and third harmonic electron cyclotron system). Starting from initial tests in 2008–2009 and continuing after being commissioned in July 2010, the new control system has seen a large number of successful

* Corresponding author at: Eindhoven University of Technology, Department of Mechanical Engineering, Control Systems Technology Group, P.O. Box 513, 5600MB Eindhoven, The Netherlands. Tel.: +31 402472839.
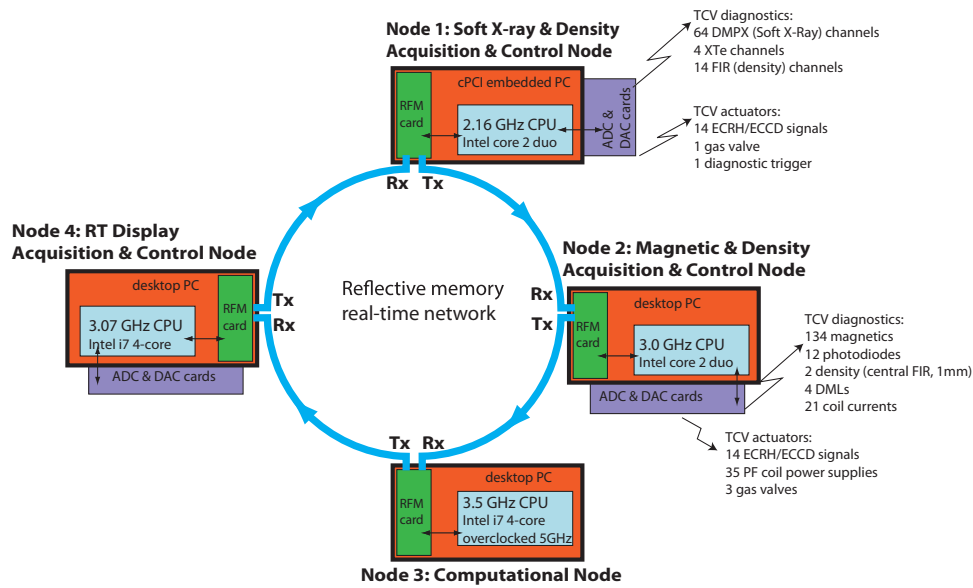E-mail address: f.felici@tue.nl (F. Felici).

Fig. 1. SCD system nodes and connections to diagnostics and actuators. Diagnostics include DMPX (soft X-rays), XTe (ratios of filtered X-ray measurements for estimating temperatures), FIR (far infrared interferometer), photodiodes (H_α light), 1 mm (interferometer), DML (diamagnetic loop) and standard magnetic diagnostics. Actuators include PF + Ohmic coils and fast internal coils for vertical stability, as well as ECRH powers and launchers. From [2,3].

applications. The hardware/software architecture of this system, known as SCD (*Système de Contrôle Distribué*) was previously outlined in [2] and is described in detail in the companion paper [3]. The present paper will exclusively treat the implemented control algorithms, and we refer the reader to the companion paper for details on the hardware, software, and real-time capability issues.

It was possible to develop many different algorithms with very limited manpower in a short time, using the possibility of programming algorithms entirely using the Simulink block programming language, i.e. without a single line of C-code. Most of the algorithms described in this paper have been used in plasma experiments that have yielded valuable insights and explored new avenues for plasma control. Details can be found in the cited references for each application.

The rest of this paper is structured as follows. Section 2 presents a brief overview of the digital control system, its architecture and programming methods. Next, Section 3 shows how the system was used to emulate the existing TCV control system, allowing backward compatibility with TCV shot preparation software. Section 4 discusses some real-time MHD detection and control algorithms. Section 5 explains how information from high-precision profile diagnostics are extracted in real-time. Section 6 briefly outlines some other applications which have been discussed elsewhere in more detail. Finally, Section 7 discusses some recent developments and plans for further use of the system's potential.

2. Overview of SCD control system and developed algorithms

2.1. Overview of the SCD control system

For completeness, we will very briefly review the architecture of the SCD control system and its interaction with other TCV control hardware. A more detailed description can be found in the companion paper [3]. The SCD is composed of a set of independent nodes (presently 4) linked via shared (reflective) memory. Each node has its own Linux-based PC, and may be equipped with ADC and/or DAC cards hosted in a Compact-PCI crate, which are in turn connected

to diagnostics and/or actuators. A list of each node's characteristics and connected actuators/diagnostics is given in Fig. 1.

The SCD can entirely control a TCV discharge, apart from the fast control loop of the in-vessel vertical stability coil (which is still handled by the analog system) and the toroidal field coils (which are driven in feedforward by a separate waveform generator). Alternatively, discharges may still be controlled by the pre-existing "hybrid" control system hardware [4]. This increases the operational flexibility of TCV so that the digital system can be run in parallel to the existing system for debugging/development.

2.2. Using Simulink for algorithm design

Algorithms to be run in the SCD control system are programmed entirely in Simulink^® [5]. All the nodes are included in a single, main Simulink model, in which each SCD node is represented as a separate subsystem. An algorithm which has to run on a specific node is programmed inside the corresponding block using standard Simulink library blocks, allowing one to use existing advanced signal processing blocks. Simple models of the process to-be-controlled are used occasionally for closed-loop simulations during algorithm development. Once the algorithm development is complete, the ensemble of nodes can then be simulated in open-loop by running the model, and data acquired from previous shots is loaded to substitute for the ADC inputs in the simulations. Controllers and data from previous shots are stored in the TCV shot database (MDSplus [6]) and can be reloaded for later use in debugging or development. This method of programming massively speeds up development, as control algorithms can be developed with continuous testing using previous shot data. During experimental operation, algorithm behavior can be simulated in open-loop just after each shot with the freshly acquired data, modified or corrected, and re-compiled between two shots. For an experienced user, this was easily possible within the 10–15 min time between two TCV shots. Compilation takes approximately 1 min and does not delay the TCV shot cycle. Compiled control algorithms are sent to each node in the form of shared object libraries, where they are executed by pre-compiled executables on each

Table 1
Example of roles of individual SCD nodes for real-time control algorithms presented in this paper, showing a variety of node clock rates depending on application requirements. This table shows just a few of the many possible combinations. Not listed are nodes RT03, which is dedicated to real-time equilibrium reconstruction, and the spare RT04 node is used for real-time display in the control room.

Algorithm	Section	Node RT01		Node RT02	
		Task	T_s (µs)	Task	T_s (µs)
Hybrid controller emulator	Section 3	Idle	–	Improved hybrid controller	100
Sawtooth and NTM control	Section 4	Sawtooth detection, control logic.	100	NTM detection, phase locking	20
ELM control	Section 4	Idle	–	ELM detection and logic	20
X-ray profile analysis and control	Section 5	RT spline fitting &control	100	Idle	–
RT profile simulation	Sections 6.2 and 7	RT-RAPTOR	900	Improved hybrid controller	100

real-time node. Details about this software integration can be found in [3].

Owing to the small amount of available manpower at TCV, the choice for SIMULINK was made at an early stage, expecting that manually developing C-code for each application would severely constrain the number of physics applications that could be developed in a short time. Starting from an algorithm design on paper, even for a relatively complex algorithm such as used for MHD control (Section 4.4), programming it in SIMULINK would take at most a couple of days, compared to the many weeks or months expected for the equivalent C-code. In all, development, implementation and experimental testing of all the algorithms mentioned in this paper required approximately 1 man-year, including TCV plasma experiments and data analysis. The resulting models resulted easy to maintain and easily transferable to other users, as well as other tokamaks which also employ SIMULINK. Given the early choice for SIMULINK, no systematic comparisons of manually generated C-code versus SIMULINK-generated C-code were made. Fortunately, in all occasions, the SIMULINK generated C-code performed as expected from off-line simulations, and resulted in sufficiently fast code for real-time use on the SCD hardware. An exception is the more recently developed real-time equilibrium reconstruction (c.f. Section 7.1), for which highly optimized C-code was developed. It should be noted that TCV being a medium-sized tokamak, code execution time constraints will be relaxed in larger tokamaks with longer time scales, which provides a further argument for the use of SIMULINK for code development.

2.3. Overview of developed algorithms

Depending on the experimental objective, different combinations of control algorithms may be used in each node. The sampling time of each node will depend on the specific algorithm used. Table 1 gives an overview of some mature applications which can be run on demand on the SCD nodes, specifying the sample time of each node and the section of this paper where each algorithm is discussed in more detail.

3. Improved TCV hybrid controller

The TCV "Hybrid" control system, originally developed as the first control system for TCV in the early 1990s, performs the basic plasma control functions of PF coil current, plasma current, plasma position, and particle density control [4]. It consists of digitally programmable analog matrix multipliers, which are programmed using the TCV shot preparation software MGAMS (Matrix Generation and Measurement Simulation) [7]. The functionality of the Hybrid control system has been replicated in the SCD, with the addition of new features which could not be handled by the analog electronics of the original system. This section describes the implementation of the emulator, and additional features.

3.1. Basic hybrid controller emulation

3.1.1. Matrices and reference signals

To understand the details of the SIMULINK emulation of the hybrid controller, more information about the TCV shot preparation procedure using MGAMS may be helpful. Starting from a time sequence of basic plasma descriptors (I_p, B_ϕ, z, κ, δ, etc.), a free-boundary code FBTE (free boundary toroidal equilibrium) [8] computes the necessary PF coil currents required to obtain the requested equilibrium. The Ohmic (OH) coil current ramp rate required to obtain the desired plasma current is included in the calculation to obtain the full set of OH and PF coil current trajectories. As the PF power supplies are generally voltage-controlled, the currents are feedback-controlled by the plasma control system itself. FBTE thus generates both coil voltage feedforward sequences and the calculated currents which are used as feedback references. These trajectories, together with reference and actuator feedforward trajectories for other controlled parameters (I_p, zI_p, radial position, density, κ), are stored in the shot database. Next, MGAMS calculates linear combinations of magnetic measurements that will be used as estimators for the shape parameters, as well as appropriate feedback gains and actuator configurations (i.e. which linear combination of coils is used to control a given shape parameter). This information is translated into a set of (possibly time-varying) coefficients for the so-called A, G, and M matrices, which are the analog matrix multiplication units that constitute the Hybrid control system. These coefficients are computed both in "physics" (MKSA) units and in "physical" (volts) units and are also stored in the shot database. When the hybrid controller is used, the physical coefficients are programmed into the analog matrices, and the time trajectories are programmed in the digital waveform generators. Time-trajectories for power and launcher angles of the ECRH system, when used, are prepared by the gyrotron operator, and similarly stored in the database before being transferred to the waveform generators.

The SIMULINK model for the SCD emulation of the hybrid control system has exactly the same layout as the physical system. The model block diagram is shown in Fig. 2. The matrices are represented by SIMULINK matrix multiplication blocks. The (time-varying) coefficients of the matrices in MKSA units are themselves loaded from the TCV database location to which they were previously stored by MGAMS during shot preparation.

3.1.2. PID transfer function discretization

The P, I and D elements of the hybrid system are implemented by analog electronic circuits which must also be converted to a digital (discrete-time) representation in SIMULINK, attempting to match their transfer functions. The frequency roll-off that was present in the analog circuits to filter out high-frequency noise does not need to be replicated in the digital system since, by nature, high frequency noise is not there if appropriate anti-aliasing filters are installed. For the proportional and integral terms, this is straightforward to achieve by taking a simple unit gain for the proportional
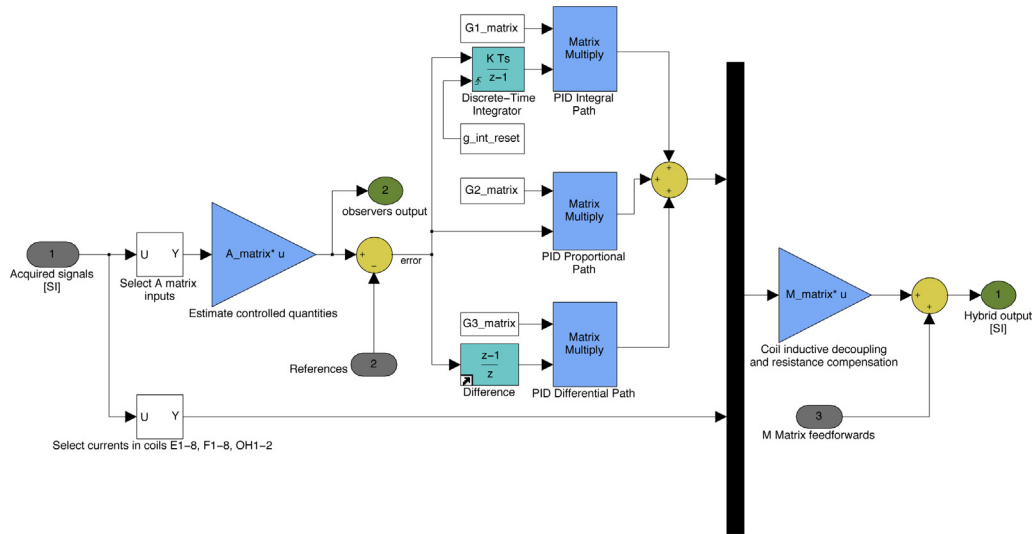
Fig. 2. Part of the SIMULINK model emulating the hybrid control system. The layout and connections in the model match the physical layout of the hybrid control system.

term $(H_P(z)=1)$ and a bilinear transform (Tustin approximation) for the integrator, with transfer function

$$H_I(z) = \frac{1+z^{-1}}{1-z^{-1}}. \tag{1}$$

The derivative term requires more care. The transfer function of the original analog electronics is, in the Laplace domain:

$$H_D(s) = \frac{s}{(1+s\tau_{D1})(1+s\tau_{D2})} \tag{2}$$

with $\tau_{D1} = 1 \times 10^{-4}$ s and $\tau_{D2} = 1.02 \times 10^{-4}$ s. This means the frequency response rolls off starting from approximately 1.6 kHz, which is a significant fraction of the Nyquist frequency (5 kHz for the standard 10 kHz sampling frequency). At these frequencies, the extra phase lag introduced by the 1-sample delay between ADC acquisition and next DAC update [3] can no longer be neglected. Since the derivative term is usually only used for the (slow) vertical control loop (i.e. the vertical position control performed by the PF coils instead of the fast internal coils), this phase lag appeared in early experiments as a reduced vertical stability ceiling, which impeded the creation of highly vertically unstable (highly elongated) plasmas. The transfer function of the analog version of the PD controller for the slow vertical control loop is plotted for shot #40476 in Fig. 3 (blue). Discretizing the controller by the Tustin approximation and adding an extra 1-sample delay, one can see that the magnitude response is close, but a significant phase lag appears (red). To remove this phase lag, the D term of the controller is rewritten as

$$H_D(z) = \frac{1-z^{-1}}{1+\alpha z^{-1}}\frac{1+\alpha}{T_s} \tag{3}$$

The factor on the right-hand-side is simply to obtain a unity time constant. The location of the denominator pole α can be varied, with $\alpha=0$ yielding a simple 1-sample difference operator. Moving the pole in the region $-1<\alpha<0$ increases the phase lag but decreases the gain, while $0<\alpha<1$ yields a phase lead and higher gain. A family of frequency responses (green) can thus be obtained, a few examples of which are shown in Fig. 3. The improved phase response comes at the expense of a higher gain at high frequencies, i.e. less noise suppression. Tuning the value of α revealed that $\alpha=0.2$ was appropriate, yielding sufficient vertical stability even for elongated shots. One must nevertheless accept a performance degradation due to the reduced noise rejection. This is inherent to the choice of a digital design. This can be reduced by increasing

the controller cycle time, but the presently used 100 μs (10 kHz) is already at the limit of the capabilities of this node for this algorithm. Alternatively, nonlinear control strategies can be envisaged [9]. Recalling that the fast vertical control loop is still handled by analog control, in the future the entire design of the vertical control loop will be reassessed taking into account the digital–analog mix of the configuration.

3.2. Improved control of the Ohmic transformer coil during non-inductive plasmas

In steady-state plasmas, the ohmic transformer coil current is clamped to a fixed value such that the plasma current it induces is truly zero. This is achieved by feedback controlling the OH coil current to a constant reference value so as to offset any drifts due to changes in the coil resistance with time as well as currents induced in the ohmic coil by another conducting elements. This mode of operation is referred to as "IOH feedback", in contrast to the standard operation of the OH coil, referred to as "I_p feedback" in which the OH coil ramp rate is feedback controlled to obtain the desired plasma current. IOH feedback is sometimes used to impose (usually small) ohmic current perturbations to steady state plasmas [10].

In the hybrid TCV controller, the OH coil current during the IOH feedback phase is pre-programmed based on the expected coil current at the moment of switching. However, if the OH coil current does not match this value at the time of switching, for example due to a different plasma resistivity in the earlier phase of the shot, the IOH current may experience a sudden jump to its pre-programmed reference which will cause a sudden spike in the induced loop voltage and may disrupt the plasma. In the past, this was alleviated by monitoring the evolution of the IOH coil current trajectories from shot to shot and adjusting the pre-programmed reference value manually. As these adjustments were made off-line, no guarantees could be given on the result.

With the advent of the SCD system, the reference adjustment can be performed online and automatically. In the digital controller, an offset is added to the reference I_{OH} at the beginning of the IOH phase in order to match the value at the switch time, thus ensuring continuity in the OH coil current evolution. This improvement is now used routinely for steady-state shots, no longer requiring manual intervention. An example of the commissioning experiments for this technique is shown in Fig. 4. This figure shows two TCV shots both of which use IOH control in the time interval between
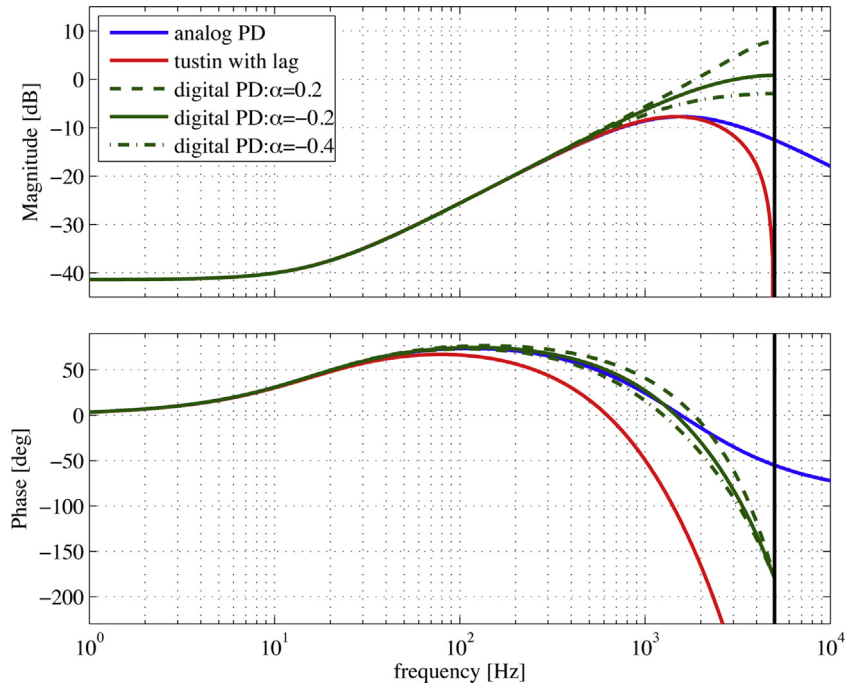
Fig. 3. Bode plot of the PD controller for the slow vertical stability loop, with gains from shot 40476. The analog transfer function implemented by the hybrid system (blue) is poorly approximated by a Tustin approximation (red) with a one-sample delay, particularly in the phase response at high frequencies. A redesign (green) of a purely digital PD controller with varying derivative pole yields a better phase response, at the cost of a higher gain close to the Nyquist frequency (black). (For interpretation of the references to color in this figure legend, the reader is referred to the web version of the article.)
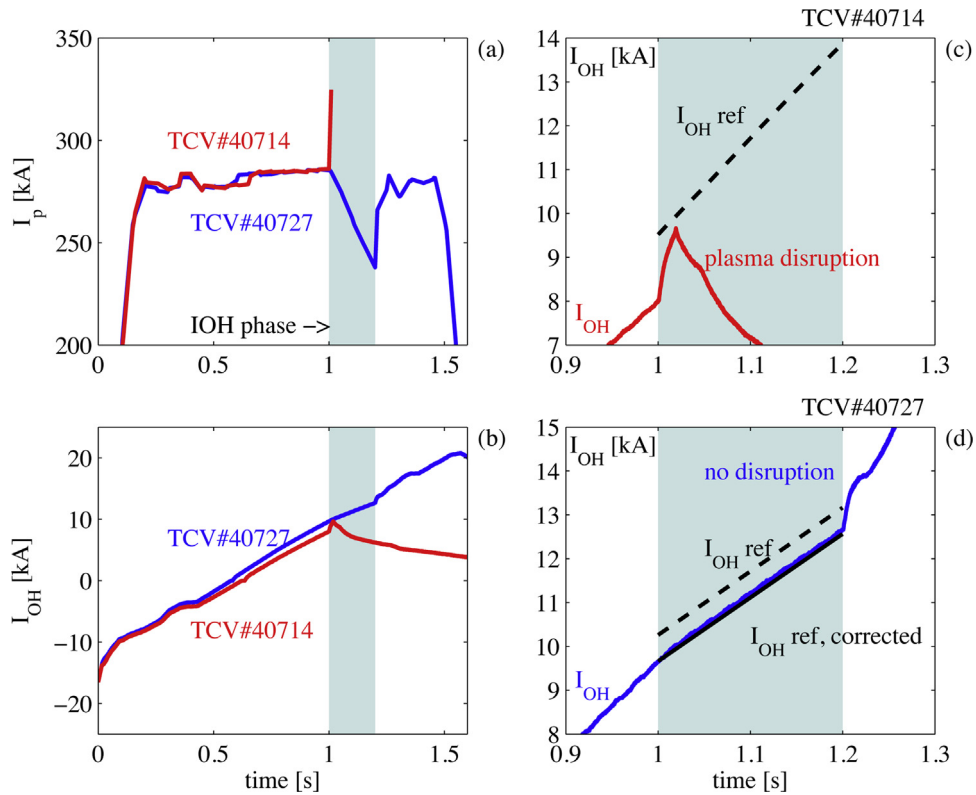

Fig. 4. Demonstration of improved IOH control (# 40727, blue) compared to the previous control (# 40714, red). By adjusting the reference OH coil current trajectory so as to start at the current value at the time of the switch from I_p to IOH feedback. For this non-steady state scenario, a ramp trajectory for I_{OH} was programmed. (For interpretation of the references to color in this figure legend, the reader is referred to the web version of the article.)
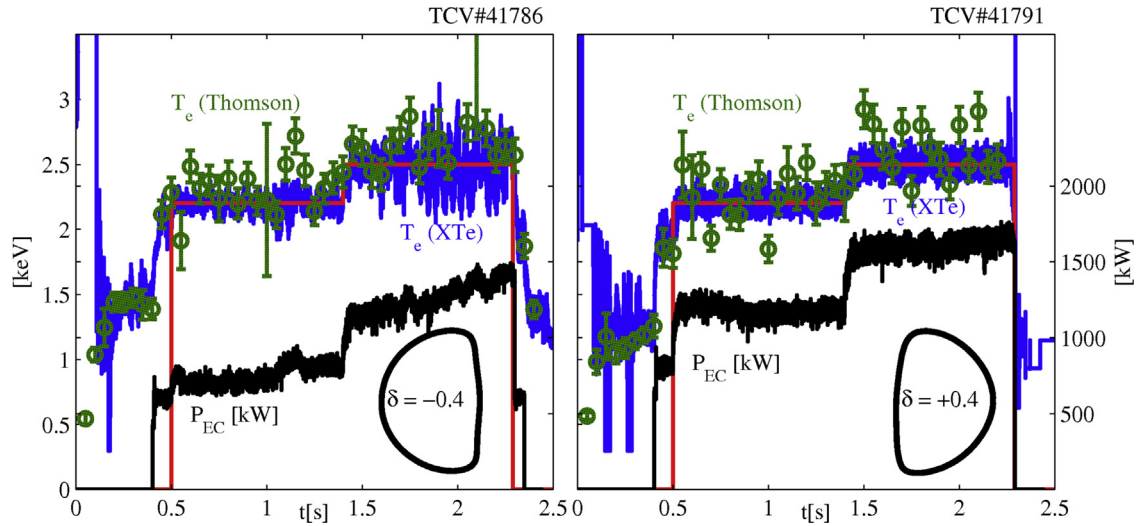
Fig. 5. Feedback control of central electron temperature by on-axis EC power in two TCV plasmas of different triangularity. In both cases, the same step from 2.2 keV to 2.5 keV is requested (red). The controller changes the power in order to match the request, needing a much lower total power level in the negative triangularity case. Post-shot measurements from the Thomson scattering diagnostic (green) are also shown, confirming the result. Note the XTe temperature estimate is not reliable in the early phases of the shot. (For interpretation of the references to color in this figure legend, the reader is referred to the web version of the article.)

$t = 1.0$ and $t = 1.2$ s (shaded region). Since this is a non-steady-state scenario, a ramp reference is programmed in order to maintain a nonzero V_{loop} and drive inductive current. In the first shot (red), the standard method is used, setting a reference trajectory for I_{OH} (panel Fig. 4(c), dashed). At the start of the IOH feedback phase, the OH coil current is about 1.5 KA lower than the first point of the reference. The current rapidly increases to match the reference, but in doing so creates a strong loop voltage which drives a strong current, Fig. 4(a), which causes a plasma disruption. In the corrected case (using SCD, blue), the original I_{OH} reference is shifted such that the first point matches the measured I_{OH} value Fig. 4(d). This gives the same loop voltage as what was programmed, but avoids unwanted V_{loop} transients. In this case the plasma does not disrupt (but I_p decreases, with the loop voltage lower than in the I_p feedback phase) and the shot proceeds normally.

3.3. Improved density control by gain scheduling

Density control in TCV is complicated by the simple fact that it is easier to add gas than to remove it due to the high recycling rate of the wall. A linear controller is therefore not well suited for this task, as the actuator response would then have the same amplitude for positive or negative error. A nonlinear controller for the plasma density has been developed [11] which uses an asymmetric gain scheduling: if the plasma density is higher than requested, the controller has a high gain and tends to close the gas valve rapidly, while for too low density the controller is more cautious in adding gas. Also, the possibility to implement anti-windup has allowed more generous use of integral control in the presence of actuator saturation (typically when the gas valve is completely closed). This simple controller has shown improved performance over the pre-existing controller and is now being transferred to a standard tool for physicists operating the tokamak.

3.4. Central electron temperature control

Experiments attempting to elucidate the turbulence phenomena underlying the cause of transport variation with shape required two plasmas with similar T_e gradient scale lengths at opposite triangularity. This was achieved by implementing a PI feedback controller for the central EC power based on the XTe diagnostic,

a multi-filter X-ray estimation of the central electron temperature [12]. The result of the controller action is demonstrated in two shots shown in Fig. 5. Here, the same reference T_e request is programmed for two plasmas of opposite triangularity. In both cases, the controller varies the EC power to obtain the requested central temperature. As can be observed from the power traces, the power required for the same temperature is lower in negative triangularity plasmas, as expected due to the improved confinement at negative triangularity [13]. A similar PI controller was also used to control the plasma β as determined from a magnetic-based real-time estimator for β [14].

4. MHD control algorithms

Next to the standard operational algorithms described in the previous section, some specific MHD control related algorithms have been implemented.

4.1. Sawtooth control

4.1.1. Sawtooth crash detection
Sawtooth crashes appear as very recognizable, sudden crashes of the core soft X-ray emissions. The rapid crashes dominate the high-frequency component of the signal, and therefore a very simple method for their detection can be based on a highpass (or bandpass) filter followed by a threshold. However, for many applications a detection trigger simultaneous to the crash is required. In many cases, the delay introduced by the high-pass filter's phase lag may be unacceptable: instantaneous or near-instantaneous crash detection is necessary based on sample-by-sample analysis. Though this boils down to a discrete-time filter in the end, the design philosophy is different. Additionally, because of the variety of sawtooth periods and crash amplitudes observed on TCV, crash thresholds should be adapted to the plasma parameters. A real-time sawtooth detector of this type was developed in the context of diagnostic triggering [15] but was subsequently used in sawtooth control experiments [16].

The detector uses the input from a single (or average) trace, referred to as y_k of the central X-ray emission, typically but not necessarily from the DMPX soft X-ray diagnostic [17], and detects a crash based on simultaneous fulfillment of two conditions:
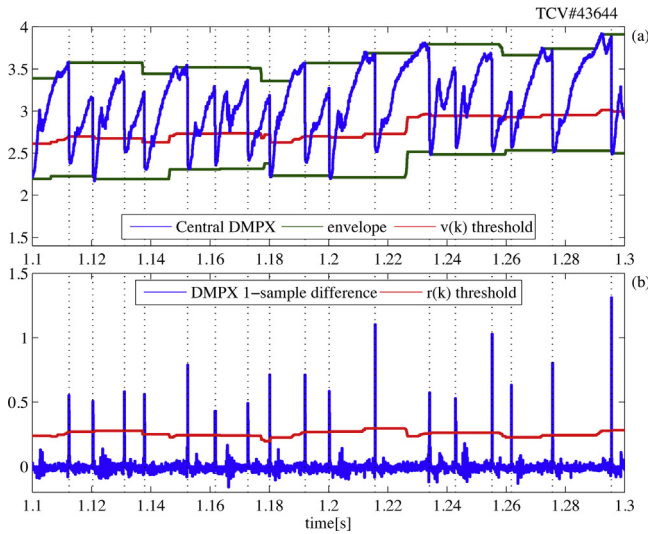
Fig. 6. Illustration of instantaneous sawtooth crash detector. A crash is detected (dotted vertical lines) when, simultaneously, (a) the DMPX signal (in arbitrary units) drops below the red $v(k)$ threshold level and (b) the 1-sample difference exceeds a threshold (red r_k). (For interpretation of the references to color in this figure legend, the reader is referred to the web version of the article.)

1 The value of the signal must cross an absolute threshold v_k in the negative direction.
2 The (negative) difference between two consecutive samples $(y_{k-1} - y_k)$ in time exceeds a given relative threshold level r_k.

The two thresholds are adapted in real-time based on the slow-scale evolution of y_k. First, an envelope for y_k is determined by storing the maximum and minimum values attained by y_k over several previous sawtooth crashes. v_k is then set to some intermediate value between this maximum and minimum. The difference threshold r_k is set to some fraction of the difference between this minimum and maximum. In practice, this provides an empirical criterion for a crash: the instantaneous change must be sufficiently abrupt and the loss of signal during the crash must be sufficiently large in order to be classified as a crash.

This method successfully rejects (i.e. does not detect) smaller crash-like events that are not full sawtooth crashes, that occasionally occur at the beginning of the sawtooth cycle: in this case the signal is either not yet above the v_k threshold and the first criterion is not satisfied, or these crashes are too slow so the second criterion is not satisfied.

An illustration of the sawtooth detector is given in Fig. 6, showing the first criterion (a) and second criterion (b) being satisfied simultaneously only for "real" sawtooth crashes. One can also see how the threshold is continually adapted to follow the global evolution of the sawtoothing signal.

A disadvantage of the present algorithm is that it is slow to adapt between very large (e.g. ECRH stabilized) sawteeth and very short (Ohmic) sawteeth, and often misses the first few Ohmic sawteeth, since the threshold values are calculated over previous sawtooth periods. Recently, a wavelet-based approach has been presented [18], which, due to its inherent multi-scale nature, may be able to simultaneously detect both small and large sawteeth without the need of adaptation.

4.2. MHD mode detection

High-frequency MHD such as tearing mode activity is also detected in real-time on TCV. This information is used in NTM control schemes described in [19] to detect the presence of a mode

before taking measures to stabilize it. The detection is based on a single magnetic probe which is, by default, connected to the RT02 node. This signal gives a typical oscillatory signal in case of MHD activity.

The detection of MHD activity from this oscillating signal can be done in a straightforward manner by bandpass filtering the magnetic signal $y(t)$ and determining its RMS power. A simple filter equation to estimate the instantaneous RMS power is

$$y_{rms}(t) = L(s)\sqrt{[B(s)y(t)]^2} \qquad (4)$$

where $B(s)$ is the transfer function of a bandpass filter – with appropriate passband for the signal of interest – and $L(s)$ is a lowpass filter with bandwidth lower than the lower limit of the passband of $B(s)$. Assuming a sinusoidally shaped signal, which is approximately true for MHD modes, the amplitude is then simply $y_{ampl} = \sqrt{2}y_{rms}$.

The appearance of an NTM is detected by a threshold on y_{ampl}. A subsequent disappearance of the mode is detected by comparing it with a (lower) threshold.

4.3. Phase-locked loop for NTM control

In addition to determining the amplitude, a phase-locked loop can be used to determine the frequency of the mode, and to generate a signal with a specified relative phase as is required, for example, for modulated ECCD injection [20]. This is described in this section. First, the bandpass filtered magnetic signal is normalized by dividing it by y_{ampl}, yielding the normalized signal $\bar{y}(t)$. Then, this signal is fed to the phase locked loop (PLL). The PLL is described by the equations

$$\omega(t) = kL(s)[y(t)c(t)] \qquad (5)$$

$$\omega_l(t) = \omega(t) + \omega_0 \quad \text{loop frequency} \qquad (6)$$

$$\phi(t) = \int \omega_l(t)\,dt \quad \text{loop phase} \qquad (7)$$

$$c(t) = \cos(\phi(t)) \quad \text{PLL oscillator output} \qquad (8)$$

Here $L(s)$ is another lowpass filter with frequency lower than the bandpass region, and k is a scalar feedback gain, and ω_0 is the rest frequency of the oscillator.

The phase difference between the locked signal $c(t)$ of the PLL and the original signal $y(t)$ is a function of the frequency due to the properties of the PLL and the phase lag induced by the bandpass filter. When the phase needs to be known exactly, for example to generate a power modulation signal with an exact phase difference with respect to the magnetic signal to use in modulated-ECCD experiments, some extra effort is needed: one takes the original signal $y(t)$ and multiplies it separately by $c(t)$ and its quadrature signal $s(t) = \sin(\phi(t))$, then lowpass filters the result. If $y(t)$ and $c(t)$ have the same frequency, i.e. the PLL is locked, then the result is $\cos(\phi_l)$ and $\sin(\phi_l)$, respectively, where ϕ_l is the instantaneous phase difference between $y(t)$ and $c(t)$. This is then recovered by $\phi_l = \tan^{-1}(\sin(\phi_l)/\cos(\phi_l))$. Based on this phase difference, other signals of arbitrary phase difference with respect to the original signal can be generated.

An example of a working PLL, implemented in SIMULINK and executed on node RT02 at 50 kHz during a TCV NTM control experiment, is shown in Fig. 7. Panel (a) shows the original signal and the amplitude estimate. Note the appearance of an NTM at $t \approx 1.1$ s and its disappearance at $t = 1.9$ s. Just below (b), the normalized and bandpass filtered signal is shown. Panels (e) and (f) show a smaller time interval of these traces, indicated by a vertical dashed line in (a–d). Fig. 7c shows the "locking indicator" signal, as discussed above this is the time derivative of the $\omega(t)$ signal. When this is close
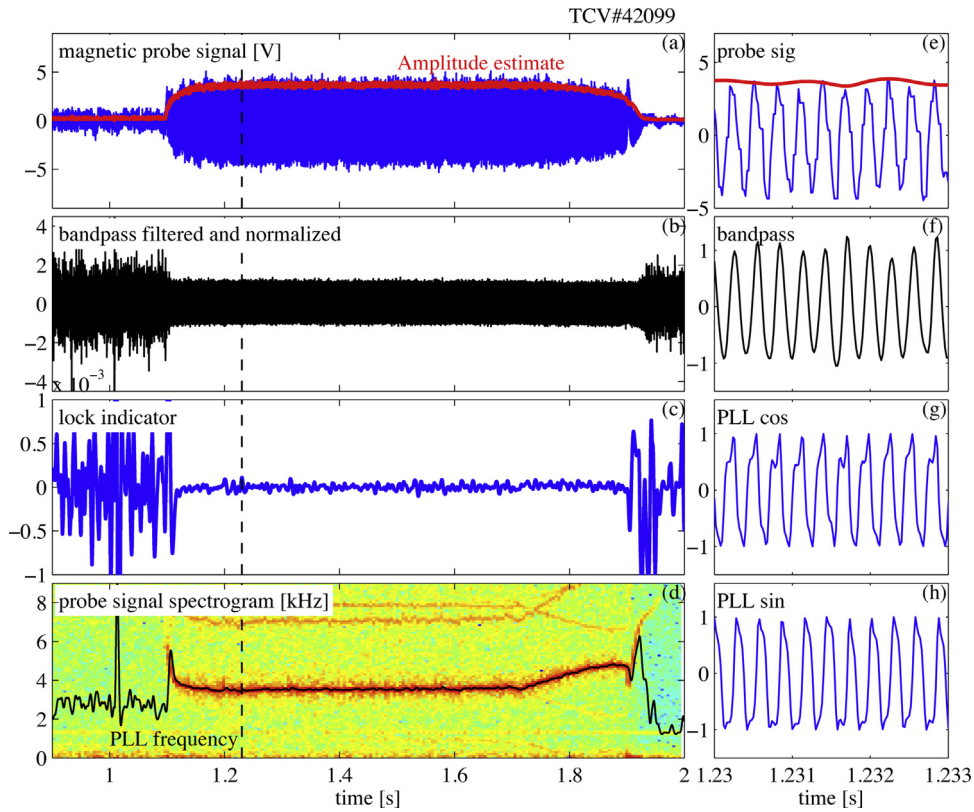
Fig. 7. Phase locked loop acting on magnetic probe signal during NTM activity from $t = 1.1$ s to $t = 1.9$ s. (Left) Raw probe signal and amplitude estimate (a), bandpass filtered and normalized signal fed to PLL (b), lock indicator signal $d\omega/dt$ (c) and spectrogram with PLL frequency estimate (d). (Right) Zoom of small time slice at dotted vertical line (e and f) and PLL in-phase and quadrature signals (g and h).

to zero, the PLL is locked. This can also be observed by comparing the mode frequency as it appears in a spectrogram (d) with the PLL frequency $\omega_l(t)$ (black line). When the PLL is locked, the frequency is observed to follow the mode frequency. Also, note how the loop tracks the varying frequency just before the mode's disappearance. Finally, (g) and (h) show the generated signals with, respectively, $0°$ (cos) and $90°$ (sin) phase difference with respect to the original probe signal. These have then been combined to generate an ECH power reference signal. Power modulation has been tested in plasma experiments and further physics studies are envisaged in the future.

4.4. Sawtooth, NTM and ELM controllers

One of the first applications of the new system was for feedback control of the sawtooth period by varying the ECCD deposition location using steerable launchers [21,22]. Later, sawtooth control by EC power was developed, notably *sawtooth pacing* [16] and demonstration of locking of the sawtooth period to modulated EC signals [23]. Similar controllers were also applied to ELM control using EC power [24,25].

The control scheme used for sawtooth pacing will be illustrated next, as it is a typical example of how an event-based control scheme can be programmed using standard SIMULINK features. Sawtooth pacing [16] relies on real-time detection of the sawtooth crash and precisely timed removal or addition of EC power near the $q = 1$ surface. This is implemented in SIMULINK by a set of counters and logic blocks as shown in Fig. 8. This diagram accepts central X-ray signals and outputs the EC power to be delivered to the $q = 1$ surface. From left to right, the X-ray signals are averaged and passed to the sawtooth detector described in the previous section. At each sawtooth, the detector sends a trigger to a counter,

which counts the time since the last sawtooth. This time is then compared to reference times for power on/off switching, which can be either pre-programmed in time or be dynamically generated from a sequence. A final block then generates the power waveform with the specified maximum and minimum powers. A final selector allows the user to switch between different modes of sawtooth control: feedforward (FF) power trace, sawtooth pacing, or fixed-period power modulation. The values of the times, powers and control modes are supplied by a signal generator block (bottom-left), in which the signals can be programmed graphically.

Experiments for study of neoclassical tearing modes were performed, in which the modes were both created and stabilized by ECRH/ECCD by varying the deposition location. A simple but robust "scan and stop" strategy was developed in which the mirror location is swept across the expected location of the magnetic island, until the island is seen to shrink or disappear. At this point, the deposition location is kept fixed, resulting in complete suppression of the magnetic island and better confinement [19]. This uses similar techniques of triggers and counters as the sawtooth pacing algorithm described above.

5. Real-time profile diagnostic analysis

5.1. Real-time profile information extraction

Profile diagnostics provide measurements at different (possibly line-integrated) spatial locations. When the spatial resolution of the diagnostic is high with respect to the feature one wishes to extract, spatial smoothing may be performed. To this end, a real-time spline fitting routine was developed. This routine exploits the fact that if the target domain on which the spline fitted values are to be computed is known in advance, the fitting operation can be rewritten
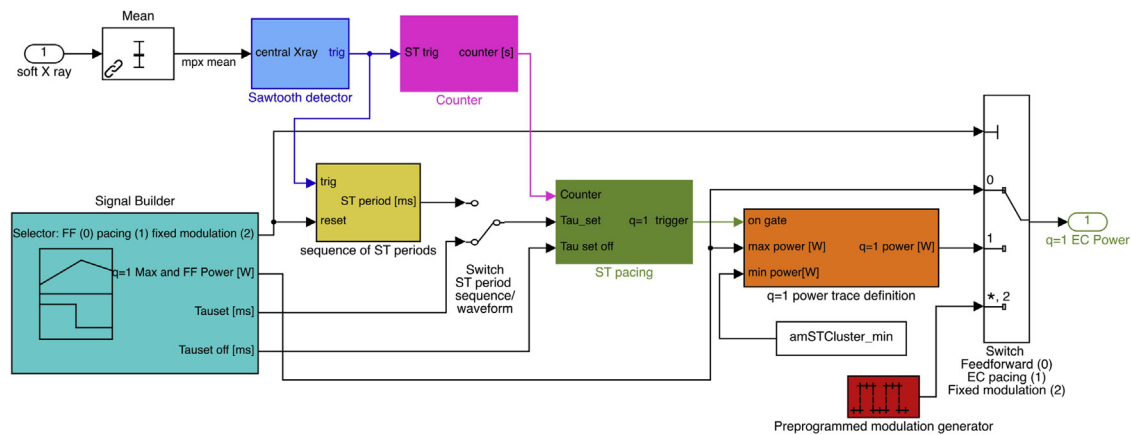
Fig. 8. SIMULINK block diagram for a sawtooth pacing controller.

into a single matrix multiplication as shown in Appendix A, the resulting matrices map the diagnostic measurements to their spline interpolated values, respectively to the derivatives of the splines (of any order) at any point. Spline interpolation and determination of profile gradients thus reduce to a set of matrix multiplication, which can easily be done in real-time. Real-time spline fitting of the 44 central channels of the 64 chord DMPX diagnostic (external channels are excluded as they are often polluted by wall effects) has been implemented for X-ray profile control experiments described in [22,26]. A typical result is shown in Fig. 9. Note that the smoothness of the spline can be adjusted by choosing a different number of piecewise polynomials.

5.2. Profile peak, width and gradient information

Based on the real-time spline interpolation routine described above, the location of the profile peak and maximum and minimum gradients can also easily be extracted. This is done simply by computing the gradients, which is also a matrix multiplication as explained in the previous section, and finding the zeros and maxima of these gradients. A typical result was already shown in Fig. 9, but is more clearly demonstrated in Figs. 10 and 11, showing spline fitted DMPX traces over time during a shot with an electron internal transport barrier (eITB), featuring an oscillatory regime [27,28] due to the interplay between MHD and transport barrier dynamics. This
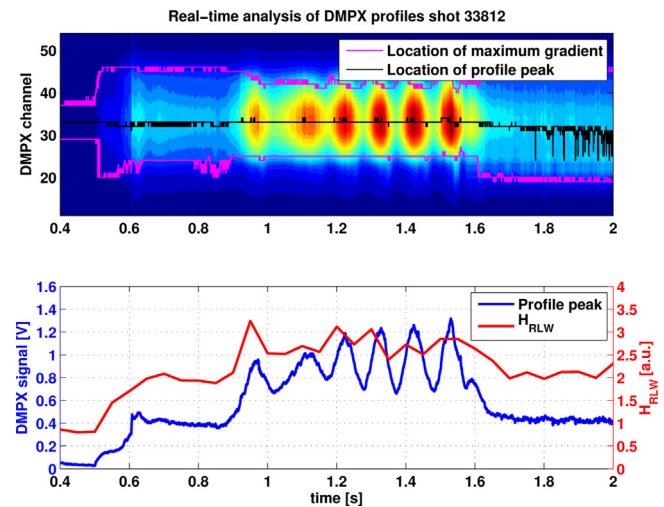

Fig. 10. (Top) Time evolution of DMPX line-integrated X-ray emissions during an oscillating eITB plasma. The location of the profile peak and location of maximum and minimum gradients, as determined by the real-time spline fitting algorithm, are also shown. (Bottom) Time evolution of peak DMPX signal and H_{RLW} (confinement enhancement factor w.r.t. RLW scaling law).
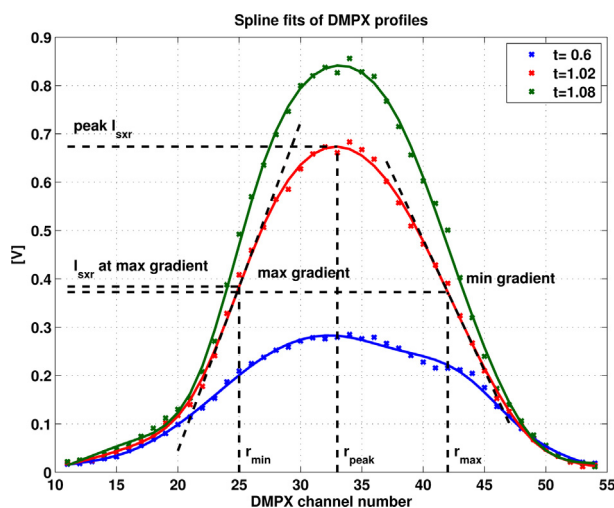

Fig. 9. Example of spline fitted DMPX profile channels, with identification of location of minimum and maximum gradients, profile peak and width. Dots represent experimental data, and curves are real-time spline fits.
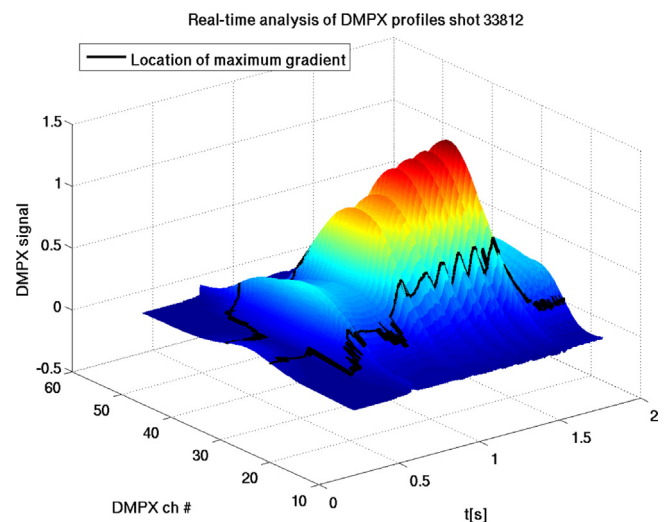

Fig. 11. 3D view of DMPX profile evolution and real-time determined minimum and maximum gradient location and value.

causes the central temperature to oscillate in a slow, periodic fashion as witnessed by the X-ray emissions. The figures illustrate how the real-time spline interpolation is able to give information about the peak location, peak value, and location of maximum and minimum gradient locations. This information is available in real-time and can be used for feedback control or other purposes.

6. Other applications

Other algorithms were developed which have been described in detail elsewhere. They are listed here for completeness.

6.1. Sliding-mode control of the plasma internal inductance

Control of the time evolution of the internal inductance during transient phases such as current ramp-up and ramp-down has been achieved using a sliding-mode controller commanding the Ohmic transformer [29]. This nonlinear controller was tuned exclusively using a previously identified dynamic model [30] and required no manual tuning during commissioning. It is worth stressing that thanks to the SIMULINK interface, development of this algorithm could be carried out remotely off-line, and since the simulation and implementation environments are identical, implementation required no additional programming.

6.2. Real-time transport simulation

One of the most advanced applications of the new system is a simulation of the current density evolution in real-time during a plasma shot [31]. This amounts to solving, in real-time, the partial differential equation for poloidal flux diffusion, using real-time measurements of the electron temperature and density to calculate the neoclassical conductivity and bootstrap current contribution. These kinetic profiles are obtained by a nonlinear (neural network) mapping from the line-integrated DMPX soft X-ray diagnostic and interferometer channels. The PDE is solved by the real-time transport code RAPTOR (RApid Plasma Transport simulatOR) [31] with a time-step of 0.9 ms, well below the current redistribution time of >100 ms in heated TCV plasmas. Knowledge of the current density distribution from the real-time transport simulation was used in a combined control of the internal inductance l_i and central temperature T_{e0} [26,32] in experiments paving the way towards future testing of full magnetic + kinetic profile controllers.

6.3. Event-based diagnostic triggering

To better study the plasma evolution during rapid plasma events (such as sawteeth or ELMs) it is advantageous to be able to take measurements at precise times relative to the event of interest. For this purpose, a real-time diagnostic triggering system was devised. A software trigger, generated by event detectors such as the one described in Section 4.1.1, is sent to an analog or digital output which triggers a diagnostic measurement. This was implemented and used in studies of ELMs using Thomson scattering diagnostic [33] and studies of momentum transport during sawteeth using charge exchange recombination spectroscopy measurements [15].

7. Outlook and work in progress

In this section we briefly outline some work in progress and future plans for advanced algorithms to be implemented in the TCV control system.

7.1. Real-time equilibrium reconstruction and shape control

Work is in progress to implement a real-time Grad-Shafranov solver in a separate computational node on the SCD control system. The solver is based on the existing off-line LIUQE equilibrium reconstruction algorithm [8], which was converted to a real-time version and re-programmed in SIMULINK using S-functions for computationally critical portions of the algorithm. Test implementation demonstrates that it is capable of providing an equilibrium every 0.7 ms. The information about the flux will be used in improved shape control algorithms in the future.

The equilibrium solver was the only application so far in which non-standard solutions had to be developed to obtain satisfactory performance. Still, it was possible to bring the code to the SIMULINK environment to maintain compatibility with the rest of the control system and to allow off-line simulations to be carried out with the equilibrium solver inside the simulation loop.

7.2. Real-time visible boundary reconstruction

To assist in plasma position/shape detection, real-time cameras are being installed with a tangential view of TCV plasmas, in which plasma boundary, diverter legs and strike points are clearly visible. The OFIT [34] algorithm will then be used to determine the location of the plasma boundary in the poloidal plane, and this information will be merged with equilibrium reconstruction. Eventually, fully optical control of the plasma boundary is envisaged, obviating the need for magnetics as may be necessary for DEMO. This information can also be used for breakdown and burn-through/ramp-up monitoring.

7.3. Real-time simulation and profile control

The real-time simulation code RAPTOR is being expanded to include a real-time sawtooth model, enabling real-time sawtooth stability analysis, prediction and control capabilities, including the effects of the sawtooth on the q-profile evolution. The real-time simulation will also be merged with real-time shape information from RT-LIUQE equilibrium reconstruction to obtain self-consistent results. The obtained q profile estimates will then be used to aim EC beams in real-time at specific rational surfaces. Collaborative research involving several institutes has also been started aimed at current density profile control integrated with real-time simulation. Controllers developed by different groups will be tested and compared in a common simulation and experimental situation to assess their merits and drawbacks.

8. Conclusions

In a relatively short amount of time, several state-of-the-art real-time plasma analysis and control algorithms have been implemented in the new "Système de Contrôle Distribué" (SCD) digital control system on the TCV tokamak. This was accomplished thanks to the fact that all algorithms are entirely designed in the SIMULINK block programming language, which allows rapid prototyping, testing with off-line data, and automatic C-code generation and compilation. The flexible nature of the SCD, which can be used to control an entire TCV discharge but can also be operated in parallel to the analog hardware-based TCV "hybrid" control system, was also instrumental to rapid development, as the SCD is not critical to operating TCV. Our experience provides a solid case for using commercial tools such as SIMULINK to design control systems. The performance of the algorithms in terms of computational speed was satisfactory in the vast majority of applications and required no further optimization or parallelization, except for complex tasks of equilibrium reconstruction where specialized solutions needed

to be developed. For larger tokamaks, where time scales are longer than on TCV, the case for using such solutions is even stronger. The compiled SIMULINK generated C-code performed exactly as expected from simulations and required no manual modification. Obtaining similar results by programming algorithms directly in C, C++ or FORTRAN, as is common practice in many devices, would have required a vastly greater effort.

The SCD control system will continue to play an important role in the TCV experimental program as more and more complex, algorithms are developed, and their use starts to become more routine and integrated into day-to-day plasma operations.

Acknowledgement

Appendix A. Real-time spline fitting

This appendix shows how to rewrite a constrained spline fitting problem on a fixed domain as a single matrix multiplication, useful for real-time implementation. Let the domain of the interpolation $x \in [a, b]$ be subdivided into n_s contiguous non-overlapping segments $x \in [x_i, x_{i+1}] \forall i = [1, \ldots, n_s]$. Next, define n_s polynomials of degree n_p: $y_i(x) = \sum_{j=0}^{n_p} a_{ij} x^j$ that take nonzero value only on $[x_i, x_{i+1}]$. Then let $y(x)$ be the piecewise polynomial obtained by joining all n_s polynomials.

Now let $y_d, x_d \in \mathbb{R}^{n_d}$ be two vectors containing, respectively, n_d data points on the interpolation domain and their corresponding x coordinate. The problem of determining the minimum square-error interpolant function $y(x)$ can be formulated as the least-squares problem

$$\min_p \| y_d - Ap \|_2^2 \tag{A.1}$$

where $p \in n_s n_p$ is a coefficient vector containing the a_{ij} and the matrix $A \in \mathbb{R}^{n_d \times n_s n_p}$ is a block-diagonal matrix with block element of the form

$$[A]_{ii} = [x_i^0, x_i^1, \ldots, x_i^{n_p}] \tag{A.2}$$

Usually, constraints are imposed to ensure continuity up to a certain derivative at the interface between the different segments. This can be rewritten as a constraint on the coefficient vector p.

$$Cp = 0 \tag{A.3}$$

with $C \in \mathbb{R}^{n_c \times n_p}$ and n_c the number of constraints. For example a $\mathcal{C}^0$ constraint (continuity) at x_2 (boundary between y_1 and y_2) is written as

$$y_1(x_2) = y_2(x_2) \rightarrow \sum_{j=0}^{n_p} a_{1j} x_2^j - \sum_{j=0}^{n_p} a_{2j} x_2^j = 0 \tag{A.4}$$

and a constraint on $\mathcal{C}^1$ (first derivative) is

$$y_1'(x_2) = y_2'(x_2) \rightarrow \sum_{j=1}^{n_p} a_{1j} j x_2^{j-1} - \sum_{j=1}^{n_p} a_{2j} j x_2^{j-1} = 0 \tag{A.5}$$

Assuming there are fewer constraints than parameters, i.e. $n_c < n_p$, the constrained least-squares problem (A.1) and (A.3) can be solved by computing an orthogonal basis for N for ker C (i.e. the null space of C, which can be computed by e.g. QR decomposition [35]). Then, write $p = Nv$ such that $CNv = 0$ for all vectors $v \in \mathbb{R}^{n_p - n_c}$. Finally one can solve the (unconstrained) least squares problem

$$\min_v \| y_d - ANv \|_2^2 \tag{A.6}$$

for example by computing the pseudo-inverse $P = (AN)^+$, the least-squares solution is $v = Py_d$.

Note that in order for a unique solution v to exist, AN must be a square or tall matrix (more rows than columns). This translates to the constraint $n_d \geq (n_p - n_c)$ which can always be satisfied for a given n_d by either decreasing the number of segments or polynomial order (lower n_p), or by adding constraints (increasing n_c).

We can now compute the polynomial coefficients of the least-squares spline interpolant to the data with a single matrix multiplication. As a last step, the values of the spline on a new set of x points is calculated by the product Dp (with matrix D of similar structure to A, but evaluated at different x values). Note also that derivatives of the spline at any point can be calculated as well, by another product denoted $D'p$

Finally the values of the interpolated spline at the required values of x are obtained directly from the original data y_d by

$$y = (DNP)y_d \tag{A.7}$$

Note that the matrix product (DNP) can be pre-calculated based solely on the knowledge of (a) the structure and order of the piecewise polynomial (b) the x coordinates of the data points (x_d), and (c) the new x points on which the interpolated spline is to be evaluated.

References

[1] F. Hofmann, J.B. Lister, W. Anton, S. Barry, R. Behn, S. Bernel, et al., Creation and control of variably shaped plasmas in TCV, Plasma Physics and Controlled Fusion 36 (12B) (1994) B277.

[2] J. Paley, S. Coda, B. Duval, F. Felici, J.-M. Moret, Architecture and commissioning of the TCV distributed feedback control system, in: Proceedings of the 17th IEEE-NPSS Real Time Conference (RT), 2010, pp. 1–6.

[3] H.B. Le, F. Felici, J.I. Paley, J.-M. Moret, B.P. Duval, S. Coda, et al., Distributed digital real-time control system for TCV tokamak, Fusion Engineering and Design (2013), http://dx.doi.org/10.1016/j.fusengdes.2013.11.001, PII: S0920-3796(13)00699-6 (in this issue).

[4] J. Lister, F. Hofmann, J.-M. Moret, F. Bühlmann, M. Dutch, D. Fasel, et al., The control of tokamak configuration variable plasmas, Fusion Science and Technology 32 (3) (1997) 321–373.

[5] http://www.mathworks.com/

[6] http://www.mdsplus.org

[7] F. Hofmann, S. Jardin, Plasma shape and position control in highly elongated tokamaks, Nuclear Fusion 30 (10) (1990) 2013.

[8] F. Hofmann, G. Tonetti, Tokamak equilibrium reconstruction using faraday rotation measurements, Nuclear Fusion 28 (10) (1988) 1871.

[9] N. Cruz, J.-M. Moret, S. Coda, J.I. Paley, B.P. Duval, A.P. Rodrigues, et al., Using APCS for plasma vertical control at TCV, IEEE Transactions on Nuclear Science 58 (2011) 1570–1575.

[10] O. Sauter, S. Coda, T.P. Goodman, M.A. Henderson, R. Behn, A. Bottino, et al., Inductive current density perturbations to probe electron internal transport barriers in tokamaks, Physical Review Letters 94 (10) (2005) 105002.

[11] W. Vijvers, F. Felici, H. Le, B. Duval, S. Coda, Non-linear digital real-time density control in the TCV tokamak, in: Proceedings of the EPS/ICPP 2012, 39th EPS Conf. on Plasma Physics 16th Int. Congress on Plasma Physics in Stockholm, Sweden, 2012.

[12] T.P. Donaldson, Theory of foil-absorption techniques for plasma X-ray continuum measurements, Plasma Physics 20 (1978) 1279–1289.

[13] Y. Camenen, A. Pochelon, R. Behn, A. Bottino, A. Bortolon, S. Coda, et al., Impact of plasma triangularity and collisionality on electron heat transport in TCV L-mode plasmas, Nuclear Fusion 47 (7) (2007) 510–516.

[14] G. Sevillano, I. Garrido, A.J. Garrido, J.A. Romero, J.I. Paley, J.-M. Moret, et al., Observer-based real-time control for the poloidal beta of the plasma using diamagnetic measurements in Tokamak fusion reactors, in: Proceedings of the 50th IEEE Conference on Decision and Control and European Control Conference, Orlando, FL, USA, 2011.

[15] B.P. Duval, A. Bortolon, L. Federspiel, F. Felici, I. Furno, T.P. Goodman, et al., Momentum transport in TCV across sawteeth events, in: Proceedings of the 23rd IAEA Fusion Energy Conference, Daejon, Korea, 2010.

[16] T.P. Goodman, F. Felici, O. Sauter, J.P. Graves, Sawtooth pacing by real-time auxiliary power control in a tokamak plasma, Physical Review Letters 106 (24) (2011) 245002.

[17] A. Sushkov, V. Andreev, Y. Camenen, A. Pochelon, I. Klimanov, A. Scarabosio, et al., High-resolution multiwire proportional soft X-ray diagnostic measurements on TCV, Review of Scientific Instruments 79 (2) (2008) 023506.

[18] M. van Berkel, G. Witvoet, M. de Baar, P. Nuij, H. ter Morsche, M. Steinbuch, Real-time wavelet detection of crashes in limit cycles of non-stationary fusion plasmas, Fusion Engineering and Design 86 (12) (2011) 2908–2919, http://dx.doi.org/10.1016/j.fusengdes.2011.07.002, ISSN: 0920-3796, http://www.sciencedirect.com/science/article/pii/S0920379611005084

[19] F. Felici, T. Goodman, O. Sauter, G. Canal, S. Coda, B. Duval, et al., Integrated real-time control of MHD instabilities using multi-beam ECRH/ECCD systems on TCV, Nuclear Fusion 52 (7) (2012) 074001.

[20] M. Maraschek, G. Gantenbein, T. Goodman, S. Günter, D. Howell, F. Leuterer, et al., Active control of MHD instabilities by ECCD in ASDEX upgrade, Nuclear Fusion 45 (11) (2005) 1369–1376.

[21] J. Paley, F. Felici, S. Coda, T.P. Goodman, F. Piras, the TCV Team, Real time control of the sawtooth period using EC launchers, Plasma Physics and Controlled Fusion 51 (5) (2009) 055010.

[22] J. Paley, F. Felici, S. Coda, T.P. Goodman, the TCV Team, From profile to sawtooth control: developing feedback control using ECRH/ECCD systems on the TCV tokamak, Plasma Physics and Controlled Fusion 51 (12) (2009) 124041 (11 pp.).

[23] M. Lauret, F. Felici, G. Witvoet, T. Goodman, G. Vandersteen, O. Sauter, et al., Demonstration of sawtooth period locking with power modulation in TCV plasmas, Nuclear Fusion 52 (6) (2012) 062002.

[24] J. Rossel, J.-M. Moret, S. Coda, O. Sauter, T. Goodman, F. Felici, et al., Edge-localized mode control by electron cyclotron waves in a tokamak plasma, Nuclear Fusion 52 (3) (2012) 032004.

[25] F. Felici, J. Rossel, B. Duval, S. Coda, T. Goodman, Y. Martin, et al., Real-time control of the period of individual ELMs by EC power on TCV, Nuclear Fusion 53 (11) (2013) 113018 http://stacks.iop.org/0029-5515/53/i=11/a=113018

[26] F. Felici, Real-Time Control of Tokamak Plasmas: From Control of Physics to Physics-Based Control, Ecole Polytechnique Fédérale de Lausanne (EPFL), Lausanne, 2011, http://dx.doi.org/10.5075/epfl-thesis-5203 (Ph.D. Thesis).

[27] V.S. Udintsev, O. Sauter, E. Asp, E. Fable, T.P. Goodman, G. Turri, et al., Global plasma oscillations in electron internal transport barriers in TCV, Plasma Physics and Controlled Fusion 50 (12) (2008) 124052 (12 pp.).

[28] G. Turri, V.S. Udintsev, O. Sauter, T.P. Goodman, E. Fable, MHD as trigger of electron temperature oscillations in ECCD discharges in TCV, Plasma Physics and Controlled Fusion 50 (6) (2008) 065010 (13 pp.).

[29] J. Romero, S. Coda, F. Felici, J.-M. Moret, G. Sevillano, I. Garrido, et al., Sliding mode control of a tokamak transformer, in: Proceedings of the 51st IEEE Conference on Decision and Control in Maui, Hawaii, USA, 2012.

[30] J. Romero, J.-M. Moret, S. Coda, F. Felici, I. Garrido, Development and validation of a tokamak skin effect transformer model, Nuclear Fusion 52 (2) (2012) 023019.

[31] F. Felici, O. Sauter, S. Coda, B. Duval, T. Goodman, J.-M. Moret, et al., Real-time physics-model-based simulation of the current density profile in tokamak plasmas, Nuclear Fusion 51 (8) (2011) 083052.

[32] F. Felici, O. Sauter, M. De Baar, S. Coda, B.P. Duval, T.P. Goodman, et al., Real-time model-based reconstruction and control of tokamak plasma profiles, in: Proceedings of the IAEA Conference 2012, San Diego, CA, USA, EX, 2012, pp. 3–12.

[33] A. Pitzschke, Pedestal Characteristics and MHD Stability of H-Mode Plasmas in TCV, EPFL, Lausanne, Switzerland, 2011 (Ph.D. Thesis).

[34] G. Hommen, M. de Baar, P. Nuij, G. McArdle, R. Akers, M. Steinbuch, Optical boundary reconstruction of tokamak plasmas for feedback control of plasma position and shape, Review of Scientific Instruments 81 (11) (2010) 113504.

[35] G.H. Golub, C.F. Van Loan, Matrix Computations, The Johns Hopkins University Press, London, UK, 1996, ISBN: 0-8018-5413-X.